A Volume-Imaging Radar Wind Profiler for Atmospheric Boundary Layer Turbulence Studies

JAMES B. MEAD,* GEOFFREY HOPCRAFT, STEPHEN J. FRASIER, BRIAN D. POLLARD, CHRISTOPHER D. CHERRY,+ DANIEL H. SCHAUBERT, AND ROBERT E. MCINTOSH

Department of Electrical and Computer Engineering, University of Massachusetts—Amherst, Amherst, Massachusetts

(Manuscript received 1 January 1997, in final form 6 October 1997)

ABSTRACT

This paper describes the turbulent eddy profiler (TEP), a volume-imaging, UHF radar wind profiler designed for clear-air measurements in the atmospheric boundary layer on scales comparable to grid cell sizes of large eddy simulation models. TEP employs a large array of antennas—each feeding an independent receiver—to simultaneously generate multiple beams within a 28° conical volume illuminated by the transmitter. Range gating provides 30-m spatial resolution in the vertical dimension. Each volume image is updated every 2–10 s, and long datasets can be gathered to study the evolution of turbulent structure over several hours. A summary of the principles of operation and the design of TEP is provided, including examples of clear-air reflectivity and velocity images.

1. Introduction

The atmospheric boundary layer (ABL) extends from the ground to the temperature inversion layer at approximately 1 km, although its upper boundary can rise several kilometers in highly convective conditions (Geernaert and Plant 1990). Within the ABL complex three-dimensional turbulent structures, driven by air–ground interaction, are associated with fluxes of heat and moisture. However, the morphology and dynamics of atmospheric turbulence are poorly understood, in large measure because instrumentation has not been available to image clear-air turbulence in multiple dimensions. In recent years, qualitative and quantitative studies of the ABL have been carried out using atmospheric computer models such as large eddy simulation (LES) (Moeng 1984; Moeng and Wyngaard 1988). LES codes are typically used to calculate the three-dimensional, time-dependent structure of the ABL, including velocity fields and local fluctuations in the structure function parameters for temperature C_T^2, humidity C_Q^2, and temperature–humidity correlation C_{TQ} (Peltier and Wyngaard 1995); those structure function parameters are proportional to C_n^2 (Wyngaard et al. 1978), which is equivalent to the radar reflectivity in the absence of precipitation or insect backscatter (Ottersten 1969). The ability of volume-imaging radars to measure three-dimensional velocity fields and local variations in C_n^2 over time can provide new insights into the structure and dynamics of the ABL and suggests that LES models may be validated or refined by comparison with radar observations.

Radar studies of clear-air turbulence began in the 1950s with efforts to understand the nature of ''radar angels'' and to explore the prevalence of clear-air scatter as a function of wavelength (Hardy and Gage 1990). By the late 1970s radar wind profilers operating at 50–3000 MHz were exploiting this phenomenon to measure winds and study turbulence at altitudes up to 20 km. Boundary layer profilers employing small antennas and low-power transmitters are effective tools for measuring winds to 5-km altitude with 100-m-height resolution. These systems typically operate near 1 GHz, which provides a good compromise between antenna size and altitude coverage (Ecklund et al. 1988).

Radar wind profilers typically support three to five fixed beams with one vertical beam and the others squinted off zenith along principal compass directions. Coherent integration followed by spectral processing of the echo signal at each range gate along each beam is used to determine the zeroth, first, and second moments of the Doppler spectrum corresponding to total power, mean velocity, and spectral width. Because the beams

* Current affiliation: Quadrant Engineering, Inc., Amherst, Massachusetts.

+ Current affiliation: MIT Lincoln Laboratories, Lexington, Massachusetts.

Corresponding author address: James B. Mead, Quadrant Engineering, Inc., 107 Sunderland Road, Amherst, MA 01002.
E-mail: mead@quad-eng.com

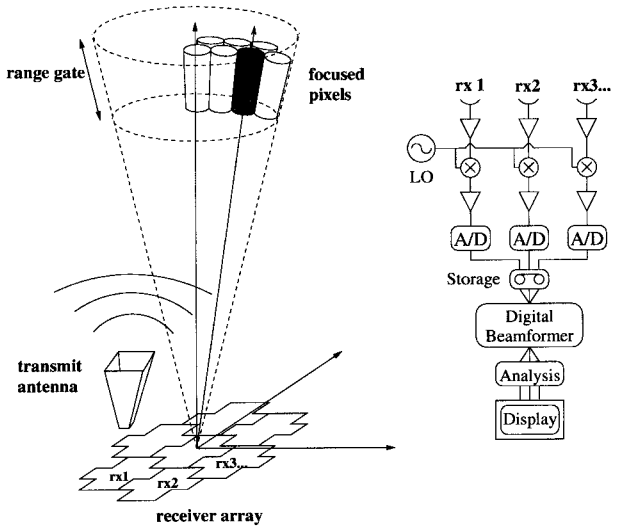

FIG. 1. Conceptual view of a digital beamforming radar system for volume imaging within the atmospheric boundary layer.

are widely spaced and somewhat coarsely sampled, it is difficult to obtain a satisfactory picture of finescale atmospheric structure necessary for LES validations. For this reason, the University of Massachusetts has developed a volume-imaging phased array radar for studying boundary layer turbulence.

The turbulent eddy profiler (TEP) is a digital beamforming phased array radar designed to provide finescale imagery of the intensity and motion of turbulence at altitudes from 200 m to 1.5 km. Digital beamforming radars employ multiple receiver elements whose outputs are processed to generate simultaneous beams within the field of view of each element. This is in contrast to active phased arrays that steer a single narrow beam varying in angle from pulse to pulse. First developed for military radar applications, digital beamforming systems have been viewed as costly and complex due to the large amount of RF and digital hardware required to sample the output of multiple antenna elements. However, the recent boom in the commercial RF market has sharply reduced the cost of microwave receivers, making it possible to consider such systems for research applications.

The TEP system may be thought of as a large collection of boundary layer profiler receivers sharing a separate transmitter antenna, as seen in Fig. 1. The signals from these individual profilers are combined in software to generate multiple narrow beams within a 28° field of view. Forming a beam at broadside is achieved by summing the complex element voltages; off-broadside beams are formed by multiplying the element voltages by an appropriate phase taper before summing. More complex adaptive processing may be used to reject interfering signals from clutter or other RF sources (Cherry 1996).

The 30-m vertical resolution of TEP is determined by the transmitted pulse length of 200 ns. Given the full array beamwidth of 3.5°, this yields volume pixels of roughly 30 m on a side at 500-m altitude—approximately equal to the grid size of LES codes. Tables 1 and 2 list the primary system characteristics.

TABLE 1. System characteristics for the turbulent eddy profiler array and transmitter systems.

General	
Nominal operating frequency	915 MHz
Range coverage	200 m to 1.6 km
Range resolution	30 m
Receive array	90-element hexagonal lattice
Array diameter	6 m
Array beamwidth	3.5°
Transmitter	
Transmit power, P_o, peak	25 kW
Pulse repetition frequency	40 kHz
Average power	200 W
Transmit antenna	Corrugated horn
Antenna/transmission line efficiency	0.9 (0.5 dB loss)
Transmit antenna 3-dB beamwidth	25°
Transmit antenna effective area, A_e	0.37 m^2

TEP is uniquely suited to measuring boundary layer phenomena that are difficult to measure with existing instrumentation. Volume-imaging lidars (Eloranta and Forrest 1992; Grund et al. 1997), capable of sampling turbulent flows over large areas, do not directly measure C_n^2. Conventional boundary layer profilers (Ecklund et al. 1988), while capable of estimating C_n^2 and mean wind velocity, are limited in spatial resolution by their broad beamwidths and coarse range resolution. The ability to simultaneously image C_n^2 fluctuations and three-dimensional velocity fields (through Doppler beam swinging) with comparatively high spatial resolution allows the motion of coherent structures to be readily visualized and studied quantitatively. Statistical analysis of the structure function data enables direct comparison with LES model statistics.

One potentially serious limitation to the ability of any clear-air radar to measure C_n^2 fluctuations is the presence of insects or other Rayleigh scatterers. Studies by Ecklund et al. (1995) and Wilson et al. (1994) suggest that

TABLE 2. System characteristics for the turbulent eddy profiler receiver and data acquisition systems.

Receivers	
LNA noise temperature	60–85 K
Receive antenna	7-element microstrip array
Antenna/transmission line efficiency	0.8 (1 dB loss)
Receive antenna 3-dB beamwidth	32°
Data acquisition system	
Digitizers	10 bit, 5 MS s^{-1}
Storage rate	2.4 MB s^{-1}
Capacity	3 h before switching tapes

particulate scattering dominates clear-air scatter in the well-mixed boundary layer, while scattering at and above the top of the boundary layer is dominated by Bragg scattering. As suggested by Ecklund et al. (1996) UHF radars may be operated in combination with a radar operating at a significantly higher frequency to determine whether Rayleigh or Bragg scattering dominates. Future field experiments with the TEP system will be carried out together with a millimeter-wave cloud radar that is highly sensitive to backscatter from insects but insensitive to Bragg scattering. This will allow identification of regions where TEP data, uncontaminated by insects, can be compared to LES models.

This paper introduces the TEP radar system and presents some preliminary results. The radar range equation relevant to TEP is presented in the following section. Section 3 summarizes the hardware design of the instrument, and section 4 presents preliminary atmospheric measurements obtained at The Pennsylvania State University's Rock Springs, Pennsylvania, field site as examples of system capabilities.

2. Range equation for volumetric beamforming array

The radar range equation for a volume-imaging beamforming radar is essentially the same as that for a conventional wind profiler (Balsley 1978), although care must be taken in using the correct effective area for the antenna:

$$\frac{S_r}{\Delta S_n} \approx \frac{P_{\text{ave}} A_{\text{et}} F_1 F_2 c\tau C_n^2 \lambda^{-1/3} \alpha_r \sqrt{N_{\text{ave}}}}{187 R^2 k (T_s + \alpha_r T_c) \sigma_{\text{fd}}}, \tag{1}$$

where $S_r/\Delta S_n$ is the ratio of signal to residual noise power spectral densities after averaging Doppler spectra and subtracting the mean noise power; P_{ave} is the average transmit power; A_{et} is the effective area of the transmit antenna; F_1 and F_2 are the fractions of received power passing through the predetection filter and coherent integrator, respectively; $c\tau/2$ is the range resolution determined by the pulse length τ and the speed of light c; C_n^2 is index of refraction structure function parameter averaged over position; λ is the free-space wavelength; α_r is the efficiency of the receive antenna and transmission line; N_{ave} is the number of spectra averaged; R is the range to the scattering volume; $k(T_s + \alpha_r T_c)$ represents the noise power density due to the receiver noise temperature T_s and the sky temperature T_c (about 80 K for an upward-looking system); k is Boltzmann's constant; and σ_{fd} is the spectral width of the received signal.

The spacing between the transmit and receive antennas (15 m) and the receiver diameter (6 m) are both a small fraction of R. Using a single value for R results in differential range errors of 2% or less for altitudes above 200 m. The spectral width of the signal is related to the wind velocity v_w and beamwidth β as well as the turbulent Doppler variance σ_{vw}^2 via

$$\sigma_{\text{fd}} = \frac{2}{\lambda}\sqrt{\sigma_{vw}^2 + [v_w \sin(\beta_f)]^2}, \tag{2}$$

where β_f is the beamwidth of the full array.

Equation (1) includes the simplification $\lambda^2 = \beta_r^2 A_{\text{er}}$, where β_r^2 is the solid angle of the receiver beam and A_{er} is the effective area of the receiver. The invariance of the product $\beta_r^2 A_{\text{er}}$ yields the result that the signal-to-noise ratio is unaffected by the size of beamforming array. In other words, the signal processing gain achieved by focusing the array is offset by the reduction in scattering volume.

Setting S_r/S_n to 1.0 and solving for C_n^2 gives noise-equivalent C_n^2 as a function of range. Figure 2 shows TEP's noise-equivalent C_n^2 between 0 and 2 km, assuming an upward-looking beam, a turbulent spectral width of 1 m s^{-1}, and a wind speed of 5 m s^{-1}. Atmospheric C_n^2 ranges from 10^{-17} on a calm, dry winter night to 10^{-12} on a warm, turbulent day in a humid environment (Gage 1990). TEP is designed for summertime operation and is able to detect values of C_n^2 as low as 5×10^{-17}.

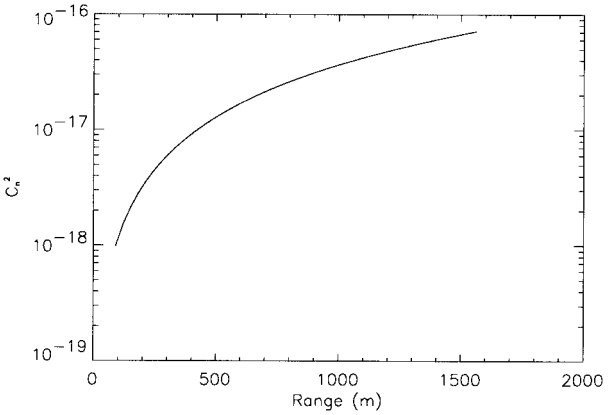

FIG. 2. Noise-equivalent C_n^2 for the zenith beam (assumptions: $v_w = 5$ m s^{-1}, $\sigma_{vw} = 1$ m s^{-1}.)

3. The turbulent eddy profiler

A site plan for TEP is shown in Fig. 3. A 48-ft-long trailer transports the entire TEP system and, during operation, houses the transmitter, data system, and host computer. A corrugated horn transmit antenna, fed by a 25-kW peak-power transmitter, illuminates a 25° wide cone above the receiver array. TEP's receiver array consists of 90 separate microstrip antennas, each backed by a low-noise receiver, digital integrator, and control and storage electronics. Coherently integrated I and Q data from each receiver is processed using a software beamforming algorithm to produce focused beams of 3.5° width, resulting in approximately 50 beams within the field of view of the radar. Figure 4 shows a photograph of the TEP array under construction in the field.

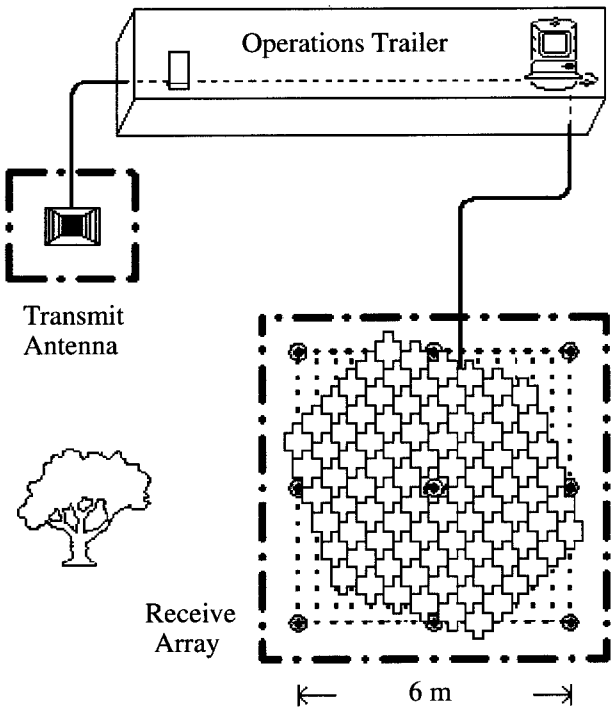

FIG. 3. TEP site plan showing relative locations of transmitter, receive array, and operations trailer.

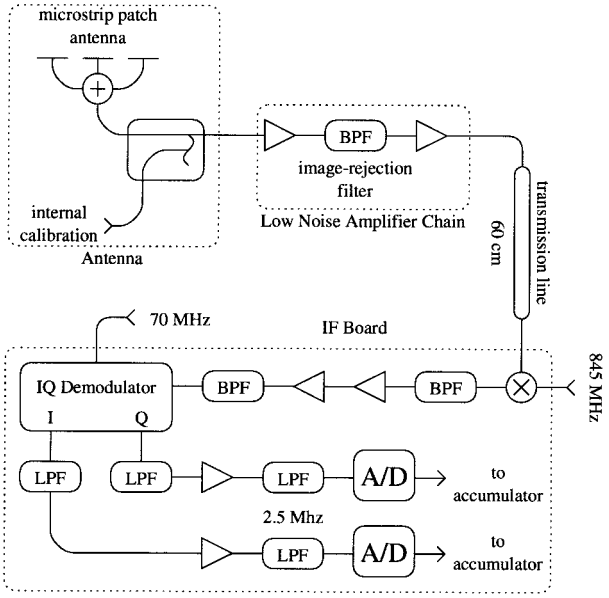

FIG. 5. Block diagram of the analog receiver circuit used in each receiver of the array.

a. Receiver system

Figure 5 is a block diagram of the analog section for the 90 receivers. A low-noise amplifier with a gain of 24 dB and a noise figure of 0.8–1.1 dB is directly attached to the antenna to minimize receiver noise power. The 70- and 845-MHz local oscillator signals are generated at the transmitter and are distributed to each receiver through a network of power dividers. The output of the analog *I*/*Q* detector is low-pass filtered to 2.5 MHz, then sampled via a pair of 10-bit analog-to-digital converters sampling at 5 MHz.

FIG. 4. TEP receive array under construction in the field. Clutter fences, the transmit horn, and the trailer are visible in the background.

The TEP receivers each sample 64 range gates at a PRF of 40 kHz. This results in a net data rate of 230 million complex numbers per second, each represented by two 10-bit integers. Clearly, all these data cannot be stored by the data acquisition system. To reduce the data rate, each receiver includes a recirculating FIFO buffer that accumulates 400 pulses at each range gate before buffering the result. A local controller then requests the data from each receiver in turn, transferring it over a fiber-optic line to a PC-mounted SCSI tape drive. Figure 6 shows a diagram of the data path. After coherent integration, the net data rate for 90 receivers is reduced to 2.4 MB s^{-1}. The maximum throughput of a PC to 8-mm tape is slightly greater than 400 kB s^{-1}, requiring a total of six separate data systems, each storing data from 15 antennas. As each tape has a capacity of 5 GB, the system can store 3.6 h of continuous data before requiring a change in tapes.

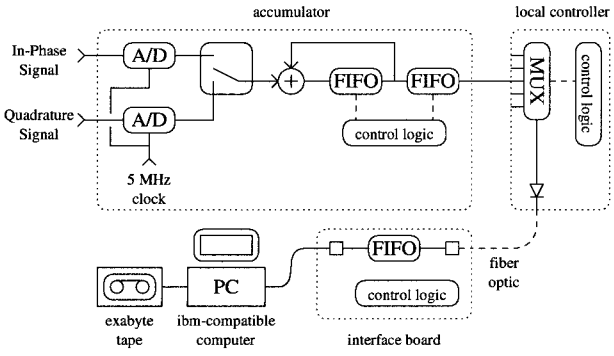

FIG. 6. Block diagram of the data acquisition system.

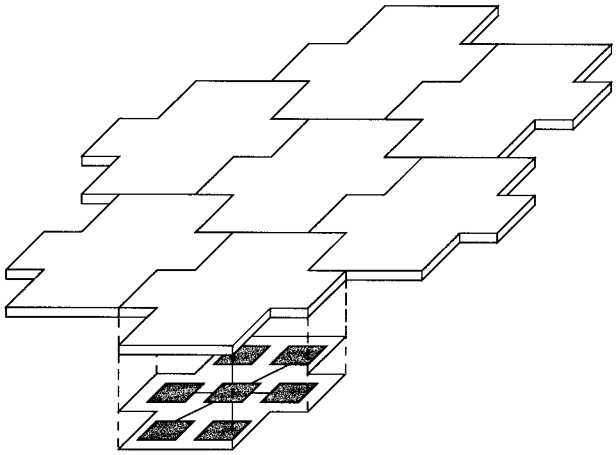

FIG. 7. Layout of an individual receiver antenna comprised of a seven-element, corporate-fed microstrip patch array over a ground plane.

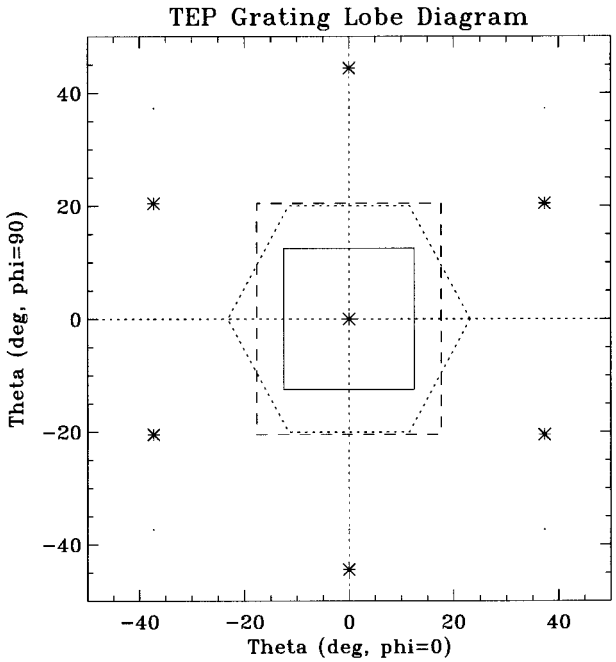

FIG. 8. Grating lobe diagram for the TEP array. Asterisks mark the locations of the main beam (origin) and grating lobes in zenith angle space. The dotted hexagon defines the boundaries of the array's available scan range. The dashed rectangle indicates the region over which beamforming is applied, while the solid rectangle defines the region retained for interpretation.

b. Transmit and receive antennas

The low radar cross section of clear air and the high clutter environment suggest the use of large aperture antennas for wind-profiling radar systems. For TEP, however, the competing requirement for a large field of view requires that individual antenna elements (both transmit and receive) have a broad beamwidth. Thus, some care is required in the design of the antennas to illuminate the volume sufficiently at broadside while rejecting clutter near endfire. A pyramidal corrugated horn was selected for the transmitter. This antenna has a main beam gain of 16 dBi with endfire sidelobes of approximately −20 dBi.

The receive antenna, shown in Fig. 7, is a suspended-substrate microstrip antenna whose half-wavelength patches exhibit nulls at endfire. Each receiver antenna is comprised of a seven-element, corporate-fed array printed on a 0.005-in.-thick fiberglass-epoxy substrate. The patches are suspended above the ground plane with a low dielectric constant foam, providing an effective relative dielectric constant of approximately 1.05. Measured antenna patterns show a symmetric 32° beam pattern with a gain of 13 dBi and endfire sidelobes of approximately −17 dBi. Addition of a clutter fence improves one-way sidelobe performance by approximately 5 dB. Resistive loss of the antenna was estimated to be approximately 0.5 dB.

The antenna element spacing in the array is 54.3 cm (1.65 λ at 915 MHz) along the principal directions of the lattice, yielding a total aperture area of 27 m^2 for 90 receivers. For the same aperture area, the hexagonal lattice permits a slightly lower sampling density than does a rectangular lattice for comparable grating lobe performance. Because the element spacing exceeds one half-wavelength, ambiguities due to grating lobes are present in the array pattern; these grating lobes are suppressed by the product of the antenna patterns of the transmit and receive elements. The product pattern has a beamwidth equal to the geometric mean of the individual patterns, yielding a 28°, two-way, 6-dB beamwidth. The grating lobe diagram for this lattice is shown in Fig. 8, where asterisks mark the locations of the main beam (origin) and the grating lobes in zenith angle space. Also shown is the array's available scan range (hexagonal region defined as half the distance to the grating lobes) and the rectangular region over which beamforming is applied. To avoid ambiguities that occur near the edge of the scan range, only a rectangular region determined by the transmitter's half-power beamwidth is retained for interpretation. At the edges of this region grating lobes are rejected by approximately 15 dB.

c. Array signal processing

Signal processing with TEP involves a combination of beamforming with spectral processing used by most conventional wind profilers. Data flow for the system is shown diagrammatically in Fig. 9. Operating on the stored data, beamforming is effectively performed 100 times per second using the 400 point sums of I and Q for each range gate of each antenna. The output of the digital beamforming algorithm is a complex voltage for each pixel. After removing DC offsets, the power spectrum of this data stream is computed for each pixel. A number of these spectra are averaged to smooth the

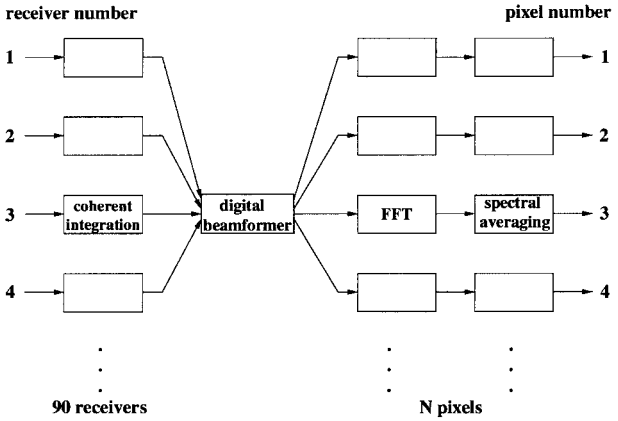

FIG. 9. Signal flow diagram showing coherent averaging, digital beamforming, and spectral processing.

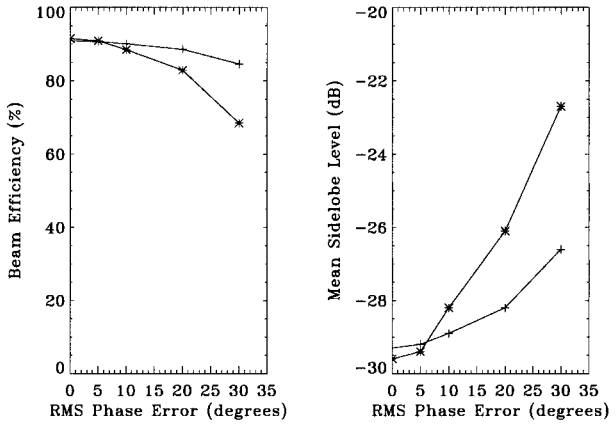

FIG. 10. Beam efficiency (left) and mean sidelobe level (right) calculated as a function of array calibration error. Plus signs indicate performance at zenith; asterisks indicate performance 12.5° off zenith.

frequency domain response. These spectra are then processed to remove clutter and any spurious signals before extracting spectral mean, spectral width, and peak power. Two-dimensional or volumetric images of any of these data products may then be generated with new images produced as often as 10 times per minute.

Beamforming involves correcting the digitized complex voltage at each element for phase and magnitude errors then summing the voltage from each element with a phase offset determined by the location of the focal point of the array, that is, the pixel location. This phase correction varies linearly across the face of the array, provided that the array is focused beyond the antenna's far field (220 m). Focusing to closer distances requires a parabolic phase correction. Phase and magnitude calibration is achieved by computing covariances of the complex signal from rain or strong clear-air scatter at adjacent antenna elements, following a procedure described in Attia and Steinberg (1989), modified for a two-dimensional array.

The most straightforward way to implement beamforming is to perform the coherent sum explicitly for every pixel, requiring N complex multiplications and additions. If the number of pixels for a given range gate is chosen to match the number of elements, then N^2 complex multiplications are required. Though computationally inefficient, this method is general, handling both near- and far-field conditions identically.

Because of the large volume of data generated by the instrument, it is desirable to exploit fast Fourier transform (FFT) techniques. If the array were arranged as a rectangular grid, then the far-field image expressed in terms of zenith angles along orthogonal directions (i.e., north–south, east–west) would simply be the 2D FFT of the array samples. The hexagonal lattice of the array, however, complicates calculation of the transform as the principal axes of the grid are nonorthogonal. A technique described in the appendix overcomes this complication with minimal computational overhead.

d. Array performance

With a quadratic aperture taper, the first sidelobe level of TEP's array factor is −23 dB relative to the main beam. Average sidelobes over the entire visible space outside of the main lobe are approximately −30 dB, setting an upper bound on the dynamic range of the image. In the absence of errors, this corresponds to a 91% broadside beam efficiency, defined here as the ratio of power within the 10-dB contours of the main lobe to the total power in the antenna pattern.

Main beam and relative sidelobe levels are modified by the composite transmitter and receiver element patterns. When the array is steered to broadside, the element patterns suppress array sidelobe (and grating lobe) energy, thereby improving beam efficiency. When steered to the edge of visible space, the main beam is attenuated by the element patterns, while array sidelobes are accentuated within the element patterns' main lobe. Thus, sidelobe rejection and beam efficiency are functions of scan angle.

Uncertainties due to gain and phase errors in the individual receiver elements will degrade sidelobe performance as well. Because TEP must be assembled in the field, proper calibration is critical to obtaining acceptable array performance. In practice, the array is calibrated either by observing a hard target such as a dipole on a balloon or by exploiting the statistical properties of the atmospheric backscatter, as suggested by Attia and Steinberg (1989). Because any such measurements are made in the presence of noise, calibrations are always subject to some error in amplitude (gain) and phase that, in turn, affect array performance.

An analysis of the beam efficiency and mean sidelobe level of the TEP array was carried out as a function of calibration error using Monte Carlo techniques. The beam efficiencies shown in Fig. 10 were computed by comparing power within the 10-dB contour of the main beam to the total power throughout the upper hemi-

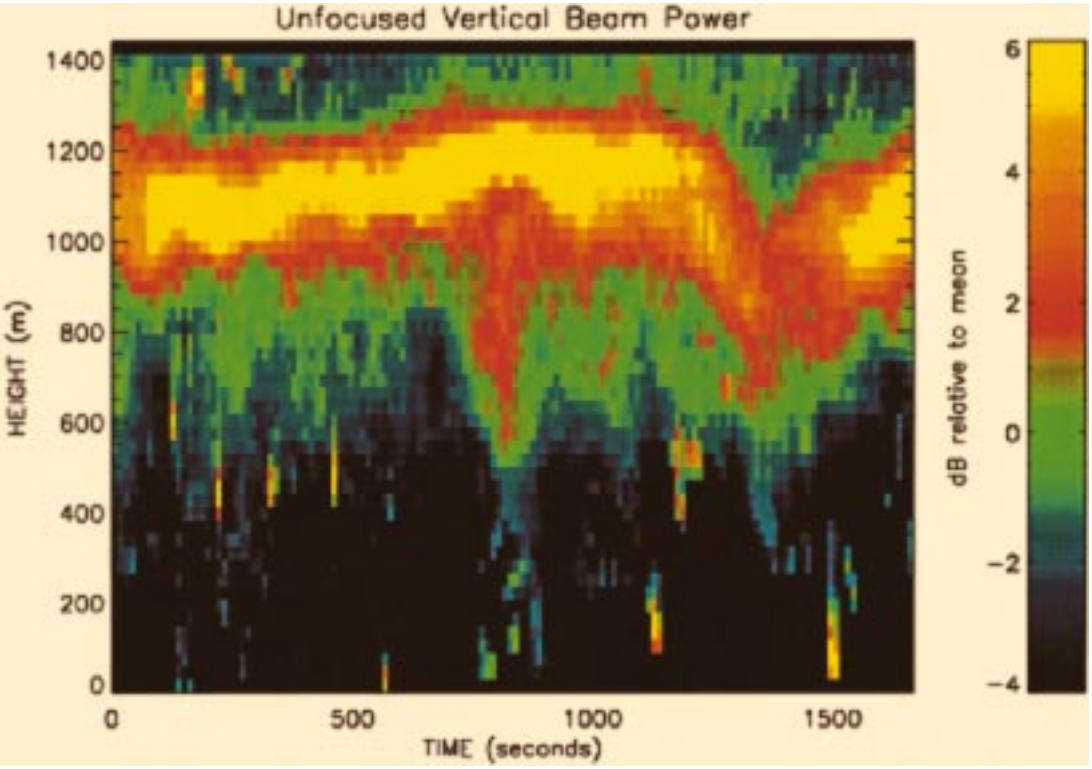

FIG. 11. Twenty-eight-min record of atmospheric backscatter observed by a single array element. Note the updraft feature near 800 s followed by the downdraft beginning at 1200 s.

sphere. Reported mean sidelobe levels are the mean values of pixels outside the 10-dB contour.

4. Sample measurements

During August 1996, TEP was deployed at the Rock Springs, Pennsylvania, field experiment facility operated by The Pennsylvania State University's meteorology department. For this deployment 60 of the 90 receivers were fielded (the outermost ring of the array was omitted). Figure 11 shows a 28-min-long height versus time profile of volume backscattering coefficient as sensed by a single element of the receiver array. The peak signal-to-noise ratio in this image is approximately 20 dB, measured at a height of 1000 m. The two-way, 6-dB beamwidth of this image is approximately 28°, as given by the geometric mean of the transmit and receiver 3-dB beamwidths. The color scale is chosen to maximize contrast of features within the boundary layer. The data were gathered on a hot August afternoon (1510 LT 22 August) with widely scattered fair weather clouds, temperature 26°C, RH = 60% with low ground winds (1.5–2 m s^{-1}) from the west.

The lowest range gates up to about 200 m are corrupted by ground clutter. The top of the boundary layer is evident at a height of between 1000 and 1200 m, indicated by a region of enhanced radar backscatter (White et al. 1991). A vertical feature evident near t = 800 s appears to elevate the top of the boundary layer. We take this to be evidence of an updraft. This is followed a few minutes later by a downdraft feature beginning at t = 1200 s, where the top of the boundary layer dips dramatically reaching a minimum at t = 1400 s.

Figure 12 displays volume images of reflectivity and velocity resolved using the focusing capability of the TEP system. Each horizontal slice corresponds to the distribution observed over the field of view for the range gate indicated on the vertical axis. An estimate of the antenna element pattern, determined by averaging power over all range gates and over time, has been removed from each image. This set of horizontal slices covers the top of the boundary layer (900–1290-m height) averaged for 5 s and corresponding to the t = 1250 s point of Fig. 11. Finer detail of the structure at the top of the boundary layer is evident, as the brightest backscatter feature follows a narrow, vertically oriented tendril shape. The corresponding Doppler images show mean Doppler velocities consistent with a downdraft in the upper range gates. In this figure, positive velocities are moving away from the radar.

A short time sequence of horizontal slices at an altitude of 1050 m is shown in Fig. 13 beginning with the time interval shown in Fig. 12. At this altitude, the range of zenith angles shown corresponds to a cross-

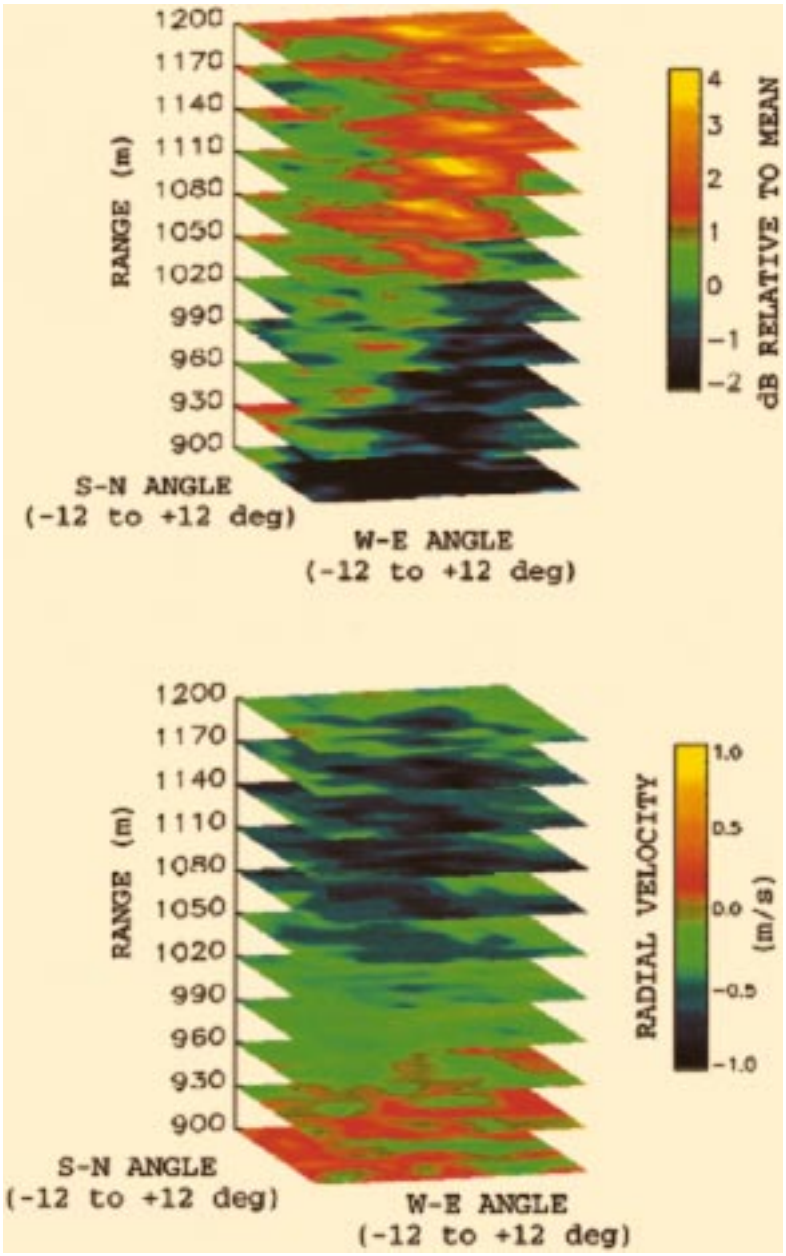

FIG. 12. Horizontal slices of the top of the boundary layer during a 5-s interval corresponding to $t = 1250$ s in previous figure. Upper plot: relative backscattered power, lower plot: mean Doppler velocity.

range distance of 460 m. The advection of the brightest reflectivity features across the field of view from west to east is readily apparent from frame to frame. The rapid evolution of the velocity field is shown by the arrows in Fig. 13, where the length of the tail indicates the magnitude of the velocity. Convergence of the velocity field in the region of strongest reflectivity is clearly apparent in this figure. The horizontal velocity vectors here are calculated using a simplification of the Velocity Azimuth Display technique, sometimes called the fixed beam Doppler method (Röttger and Larsen 1990). Each velocity pixel represents an average over a 5×5 grid, equivalent to 9° resolution.

Figure 14 shows a rendered three-dimensional volume derived from the crosswind slice of the TEP field of view as a function of time. This image was produced by casting rays through the volumetric data and reporting the maximum intensity observed along each ray. Two small gaps in the data of 70 s each occurred at 700 and 1400 s, which we assumed was zero length in pro-

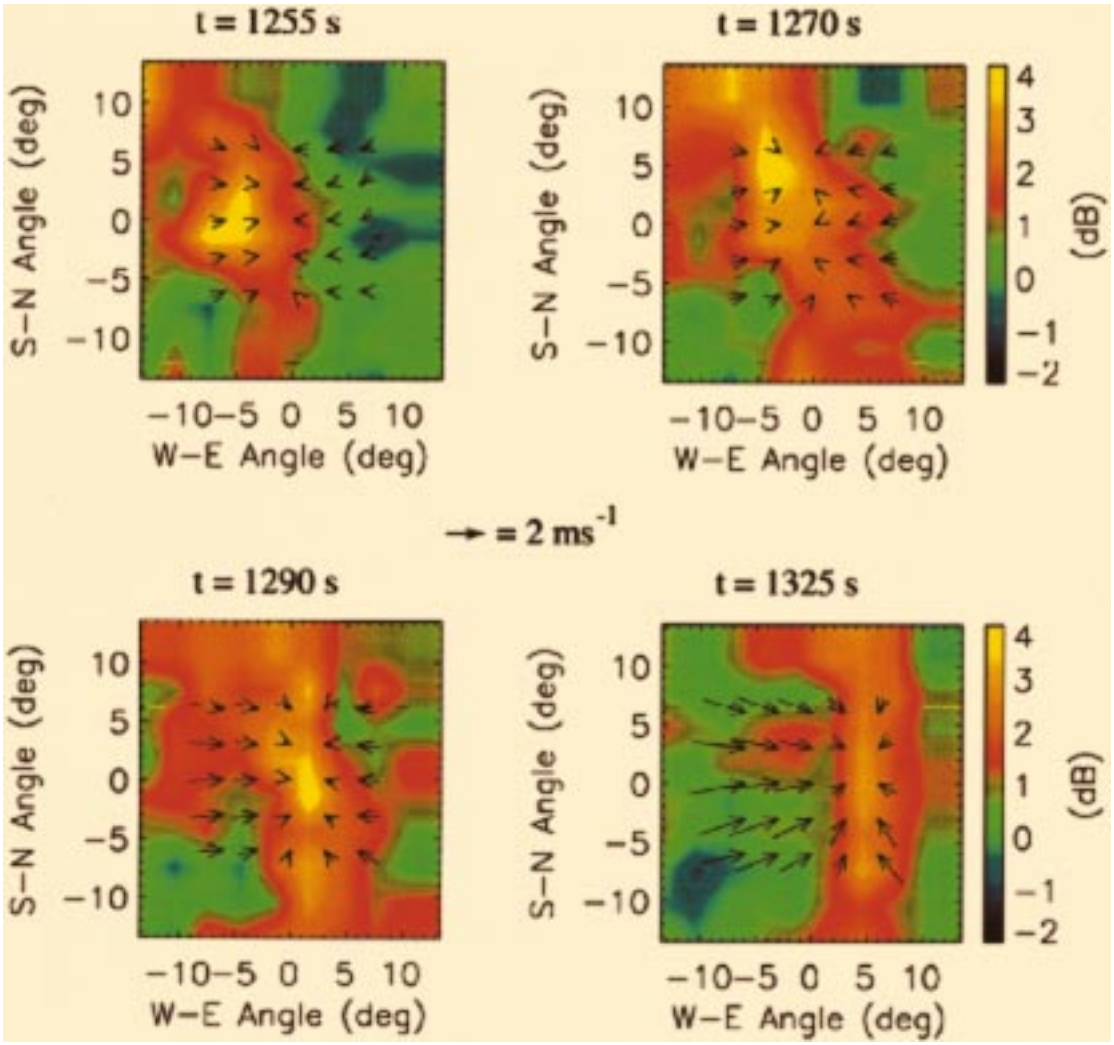

FIG. 13. Short time sequence of backscatter and velocity within a single horizontal slice at 1050-m height.

cessing the image. Data in such a format are useful for qualitative comparison and validation of LES models that produce predictions on a similar sized grid.

5. Discussion

The data presented above demonstrate that digital beamforming radar techniques can be successfully applied to clear-air scattering applications. Although the data presented above has features that are clearly connected to convective processes, it is still unclear to what degree the reported C_n^2 data are contaminated by Raleigh scattering from insects. Future field experiments will include simultaneous millimeter-wave cloud radar observations to estimate the radar cross section of insects or other particulates at various altitudes.

While a direct comparison of atmospheric features between TEP and LES output is not feasible, statistical comparisons of local fluctuations of C_n^2 are currently being investigated. Peltier and Wyngaard (Peltier and Wyngaard 1995) defined ''local'' C_n^2 values from pixel-sized, volume-averaged quantities available from LES; such values will be statistically compared to TEP measured values. Other comparisons will include three-dimensional velocity fluctuations and eddy dissipation rates from TEP and LES.

Acknowledgments. The authors gratefully acknowledge D. W. Thomson and J. C. Wyngaard of The Pennsylvania State University for their support of field measurements, and the efforts of K. Tuttle, M. Leng, and E. Knapp of the University of Massachusetts. This work was supported by the U.S. Army Research Office under Grant DAAL03-92-G-0110. Any opinions, findings, and conclusions or recommendations expressed in this material are those of the authors and do not necessarily reflect the views of the Army Research Office.

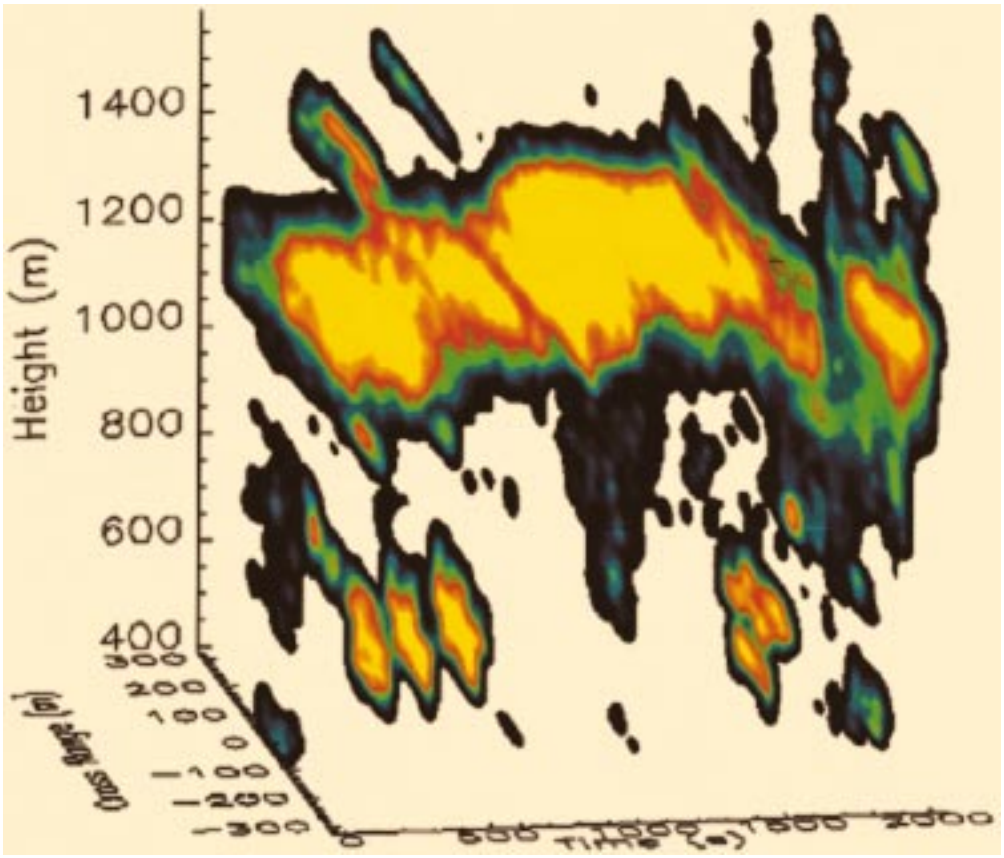

FIG. 14. Cross-wind vertical slice as a function of time rendered as a 3D volume. The long axis represents a 28-min time series converted to distance assuming a 2 m s^{-1} wind speed.

APPENDIX

Array Processing

The hexagonal array may be viewed as a subset of an $M \times N$ parallelogram of grid points, as shown in Fig. A1. For a planar array lying on the x–y plane, the far-field pattern is expressed in terms of the Fourier transform relation

$$F(u, v) = \sum_{m=0}^{M-1} \sum_{n=0}^{N-1} a(m, n) I(m, n) e^{-jkx_{mn}u} e^{-jky_{mn}v}, \quad \text{(A1)}$$

where $u = \sin\theta \cos\phi$, and $v = \sin\theta \sin\phi$; θ and ϕ are the respective zenith and rotation angles in a conventional spherical coordinate system (θ measured positive from the z axis, ϕ measured positive counterclockwise from the x axis). The arcsines of u and v correspond to zenith angles projected along the x and y axes, respectively. The $I(m, n)$ represent the array element excitations, $a(m, n)$ are weights for shaping the beam, k is the radar wavenumber, and the element locations are given by

$$x_{mn} = md_x + nd_y \operatorname{cotan}\alpha \quad \text{(A2)}$$

and

$$y_{mn} = nd_y, \quad \text{(A3)}$$

where d_x and d_y are the spacings of the elements along the x and y axes, respectively, and α is the angle between principal directions of the lattice, as shown in Fig. A1. Substituting these in (A1) yields an expression of the form

$$F(u, v) = \sum_{n=0}^{N-1} w_u(n) G_u(n) e^{-jknd_y v}, \quad \text{(A4)}$$

where the $G_u(n)$ represent the (one-dimensional) Fourier transform sums over m and the $w_u(n)$ represent a complex modulation signal given by

$$w_u(n) = e^{-jknd_y \operatorname{cotan}(\alpha) u}. \quad \text{(A5)}$$

By virtue of the Fourier transform, this modulation term applied to the u-domain signal is equivalent to a linear shift of the array samples by nd_y cotanα in the x domain. Since the modulation frequency is a function of n, it has the effect of aligning the data in the x-direction Fourier transforms, such that Fourier transform sums over n now correspond to transformations from the y domain to the v domain.

Machine computation of the far field involves a sequence of N FFTs of M points along the m dimension of the array, followed by MN complex multiplies for the modulation, followed by M FFTs of N points along

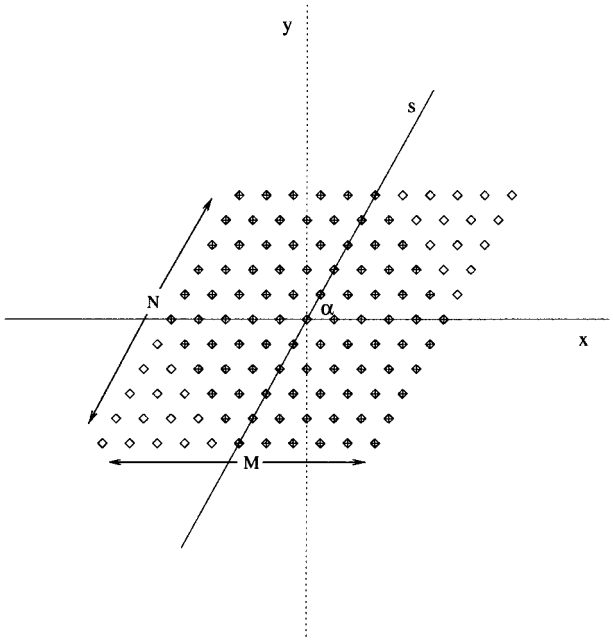

FIG. A1. Hexagonal array as part of a skewed Cartesian grid of points.

the *n* dimension. The entire operation is preceded by *MN* complex multiplies for tapering the array. An operation count is approximately $(MN/2)\log_2(MN) + 2MN$ for *MN* equals a power of 2. A 90-element hexagonal array fits within an 11×11 matrix, so choosing a 16×16 array for FFT processing yields an operation count of 1536 for 256 pixels spanning the scan range of the array (compare to 8100 complex operations for 90 pixels obtained via simple summing). Alternatively, a mixed radix FFT routine operating on a 12×12 array yields a similar operation count for 144 pixels. Further improvement in speed may be possible by resorting to so-called hexagonal FFT (HFFT) algorithms, as described by Mersereau (1979).

Fourier transform methods handle the beamforming problem for far-field conditions only. Near-field (Fresnel region) focusing is achieved by applying a quadratic phase taper to the array prior to beamforming via FFTs. In practice, such a correction is incorporated into an overall array calibration vector including corrections for antenna gain and phase errors and the amplitude taper $a(m, n)$.

REFERENCES

Attia, E. H., and B. D. Steinberg, 1989: Self-cohering large antenna arrays using the spacial correlation properties of radar clutter. *IEEE Trans. Antennas Propag.*, **37,** 30–38.

Balsley, B., 1978: Design considerations for coherent radar systems for probing the troposphere, stratosphere, and mesosphere. Preprints, *18th Conf. on Radar Meteorology,* Atlanta, GA, Amer. Meteor. Soc., 387–390.

Cherry, C., 1996: Digital and adaptive beamforming techniques for environmental remote sensing applications. Ph.D. thesis, University of Massachusetts, 190 pp.

Ecklund, W. L., D. Carter, and B. Balsley, 1988: A UHF wind profiler for the boundary layer: Brief description and initial results. *J. Atmos. Oceanic Technol.*, **5,** 432–441.

——, P. E. Johnston, W. L. Clark, J. M. Warnock, T. E. VanZandt, and K. S. Gage, 1995: Scattering from clear air, precipitation, and biological targets: Multiple frequency profiler studies. *Proc. Seventh MST Radar Workshop,* Hilton Head, SC, Solar-Terrestrial Energy Program, 32–35.

Eloranta, E. W., and D. K. Forrest, 1992: Volume-imaging lidar observations of the convective structure surrounding the flight path of a flux-measuring aircraft. *J. Geophys. Res.*, **97,** 18 383–18 393.

Gage, K. S., 1990: Radar observations of the free atmosphere: Structure and dynamics. *Radar in Meteorology,* D. Atlas, Ed., Amer. Meteor. Soc., 534–574.

Geernaert, G. L., and W. J. Plant, 1990: *Surface Waves and Fluxes.* Vol. 1. Kluwer Academic, 372 pp.

Grund, C. J., and Coauthors, 1997: The high resolution Doppler lidar: A new tool for boundary layer research. Preprints, *12th Symp. on Boundary Layers and Turbulence,* Vancouver, BC, Canada, Amer. Meteor. Soc., 15–16.

Hardy, K. R., and K. S. Gage, 1990: The history of radar studies of the clear atmosphere. *Radar in Meteorology,* D. Atlas, Ed., Amer. Meteor. Soc., 130–142.

Mersereau, R. M., 1979: The processing of hexagonally sampled two-dimensional signals. *Proc. IEEE,* **67,** 930–949.

Moeng, C. H., 1984: A large eddy simulation model for the study of planetary boundary-layer turbulence. *J. Atmos. Sci.*, **41,** 2052–2062.

——, and J. C. Wyngaard, 1988: Spectral analysis of large eddy simulations of the convective boundary layer. *J. Atmos. Sci.*, **45,** 3574–3587.

Ottersten, H., 1969: Radar backscattering from the turbulent clear atmosphere. *Radio Sci.*, **4,** 1179–1193.

Peltier, L. J., and J. C. Wyngaard, 1995: Structure-function parameters in the convective boundary layer from large eddy simulation. *J. Atmos. Sci.*, **52,** 3641–3660.

Röttger, J., and M. F. Larsen, 1990: UHF/VHF radar techniques for atmospheric research and wind profiler applications. *Radar in Meteorology,* D. Atlas, Ed., Amer. Meteor. Soc., 235–281.

White, A. B., C. W. Fairall, and D. W. Thomson, 1991: Radar observations of humidity variability in and above the marine atmospheric boundary layer. *J. Atmos. Oceanic Technol.*, **8,** 639–658.

Wilson, J., T. Weckwerth, J. Vivekanandan, R. Wakimoto, and R. Russell, 1994: Boundary layer clear-air radar echoes: Origin of echoes and accuracy of derived winds. *J. Atmos. Oceanic Technol.*, **11,** 1184–1206.

Wyngaard, J., W. T. Pennell, D. H., Lenschow, and M. A. LeMone, 1978: The temperature-humidity covariance budget in the convective boundary layer. *J. Atmos. Sci.*, **35,** 47–58.